Title

Asynchronous x-ray multiprobe data acquisition for x-ray transient absorption spectroscopy

Journal

Review of Scientific Instruments, 94(1)

ISSN

0034-6748

Authors

Kinigstein, Eli Diego
Otolski, Christopher
Jennings, Guy
et al.

Publication Date

2023

DOI

10.1063/5.0100596

Peer reviewed

Review of Scientific Instruments

Asynchronous x-ray multiprobe data acquisition for x-ray transient absorption spectroscopy

Cite as: Rev. Sci. Instrum. **94**, 014714 (2023); https://doi.org/10.1063/5.0100596
Submitted: 25 May 2022 • Accepted: 05 January 2023 • Published Online: 27 January 2023

Eli Diego Kinigstein, Christopher Otolski, Guy Jennings, et al.

AIP Publishing

Review of Scientific Instruments ARTICLE scitation.org/journal/rsi

Asynchronous x-ray multiprobe data acquisition for x-ray transient absorption spectroscopy

Cite as: Rev. Sci. Instrum. 94, 014714 (2023); doi: 10.1063/5.0100596
Submitted: 25 May 2022 • Accepted: 5 January 2023 •
Published Online: 27 January 2023

Eli Diego Kinigstein,[1,2,a)] Christopher Otolski,[3] Guy Jennings,[1] Gilles Doumy,[3] Donald A. Walko,[1] Xiaobing Zuo,[1] Jinghua Guo,[2] Anne Marie March,[3] and Xiaoyi Zhang[1,a)]

AFFILIATIONS

[1]X-ray Science Division, Advanced Photon Source, Argonne National Laboratory, 9700 S. Cass Ave., Lemont, Illinois 60439, USA
[2]Advanced Light Source, Lawrence Berkeley National Laboratory, Berkeley, California 94702, USA
[3]Chemical Sciences and Engineering Division, Argonne National Laboratory, 9700 S. Cass Ave., Lemont, Illinois 60439, USA

[a)]**Authors to whom correspondence should be addressed:** eli.kinigstein@lbl.gov and xyzhang@anl.gov

ABSTRACT

Laser pump X-ray Transient Absorption (XTA) spectroscopy offers unique insights into photochemical and photophysical phenomena. X-ray Multiprobe data acquisition (XMP DAQ) is a technique that acquires XTA spectra at thousands of pump-probe time delays in a single measurement, producing highly self-consistent XTA spectral dynamics. In this work, we report two new XTA data acquisition techniques that leverage the high performance of XMP DAQ in combination with High Repetition Rate (HRR) laser excitation: HRR-XMP and Asynchronous X-ray Multiprobe (AXMP). HRR-XMP uses a laser repetition rate up to 200 times higher than previous implementations of XMP DAQ and proportionally increases the data collection efficiency at each time delay. This allows HRR-XMP to acquire more high-quality XTA data in less time. AXMP uses a frequency mismatch between the laser and x-ray pulses to acquire XTA data at a flexibly defined set of pump-probe time delays with a spacing down to a few picoseconds. AXMP introduces a novel pump-probe synchronization concept that acquires data in clusters of time delays. The temporally inhomogeneous distribution of acquired data improves the attainable signal statistics at early times, making the AXMP synchronization concept useful for measuring sub-nanosecond dynamics with photon-starved techniques like XTA. In this paper, we demonstrate HRR-XMP and AXMP by measuring the laser-induced spectral dynamics of dilute aqueous solutions of $Fe(CN)_6^{4-}$ and $[Fe^{II}(bpy)_3]^{2+}$ (bpy: 2,2′-bipyridine), respectively.

I. INTRODUCTION

X-ray Transient Absorption (XTA) spectroscopy measures small, dynamic changes in the x-ray absorption spectrum caused by the photoexcitation of a sample with a short laser pulse. This technique provides information about the oxidation state and coordination geometry of the photoexcited species. Here, we define the XTA spectrum $\Delta S(\Delta t, E)$ as

$$\Delta S(\Delta t, E) = S(\Delta t, E) - S(E)_{GS}, \quad (1)$$

where $S(\Delta t, E)$ is the fluorescence-detected x-ray absorption spectrum (f-XAS) of the sample at pump-probe time delay Δt after laser excitation. $S(E)_{GS}$ is the ground-state f-XAS of the sample measured before laser excitation.

X-ray Multiprobe data acquisition[1] (XMP DAQ) is a technique for XTA spectroscopy that measures probe data from every time-delayed x-ray pulse after the laser, in a single acquisition. This allows efficient observation of XTA spectral dynamics over a broad temporal range (~100 μs), making XMP DAQ an ideal tool for characterizing light induced processes across relatively long time scales[2–7] such as diffusion-limited photochemical reactions. Figures 1(a) and 1(b) illustrate the pump-probe synchronization concept employed in previous implementations of XMP DAQ. The black line in Fig. 1(a) shows the sample dynamics resulting from laser excitation, while the red dotted line represents the laser pump pulse. Figure 1(b) shows the synchronized x-ray probe pulses. The first x-ray probe pulse after the laser provides a single XTA "snapshot" of fast photophysical processes (on the 50–100 ps time scale), while the subsequent photoexcited sample dynamics are obtained in a set of XTA measurements at pump-probe time delays Δt_n given by

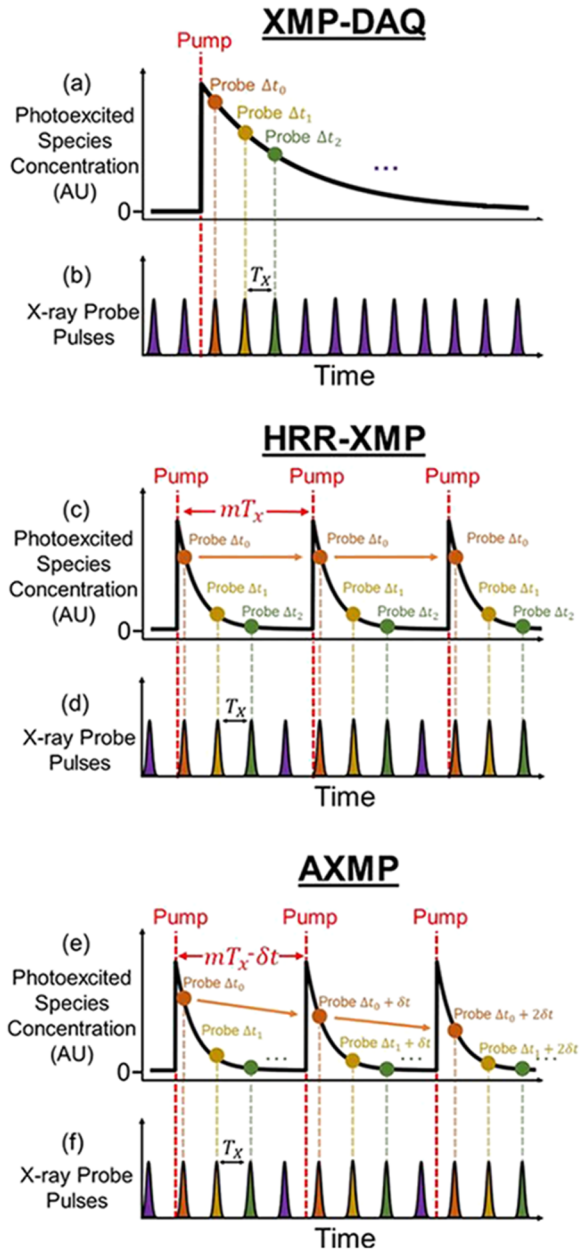

FIG. 1. A schematic illustration of the pump-probe synchronization scheme used in XMP DAQ [panels (a) and (b)], HRR-XPM [panels (b) and (c)], and AXMP [panels (e) and (f)]. Panels (a), (c), and (e) show the concentration of photoexcited species at a function of time under different laser excitation conditions. Panels (b), (d), and (f) show the corresponding x-ray probe pulses and their delays to the pump laser.

$$\Delta t_n = \Delta t_0 + nT_X, \tag{2}$$

where Δt_0 is the time delay between the pump laser and the following x-ray probe pulse, and n is an integer. The first three x-ray probe pulses after the laser are indicated by the color-coded peaks in Fig. 1(b), while the matching circles in Fig. 1(a) show the concentration of photoexcited species probed by each x-ray pulse.

XMP DAQ acquires highly self-consistent XTA dynamics by effectively cycling through measurements at every pump-probe time delay and recording these data in a single measurement. This scheme ensures that the XTA data collected at each Δt_n are obtained under nearly identical experimental conditions on average. In contrast, when acquiring XTA kinetics in a series of measurements at individual time delays, low frequency noise in the experimental apparatus, such as technical noise and signal drift, can lead to an unacceptable ambiguity between real sample dynamics and experimental artifacts.[8,9] The XMP DAQ technique mitigates the effects of signal drift, enabling the acquisition of highly self-consistent XTA data.

The high quality XTA kinetics obtained with XMP DAQ motivates expanding its technical capabilities. In this work, we present two new techniques for XTA data acquisition that use the XMP DAQ framework but are optimized to measure XTA dynamics in different temporal regimes: (1) High Repetition Rate X-ray Multiprobe (HRR-XMP), which is designed to increase the achievable signal-to-noise ratio (SNR) of the XTA measurement over time scales between 1 and tens of ns and (2) Asynchronous X-ray Multiprobe (AXMP) data acquisitions, which are more suitable to study XTA dynamics on the sub-ns time scale.

HRR-XMP is a combination of the high repetition rate XTA technique[10–13] with XMP DAQ and is depicted in Figs. 1(c) and 1(d). The high laser repetition rate improves the signal statistics acquired at each time delay.[10–13] For example, the three closely spaced laser pulses in Fig. 1(c) enable three identical measurements of the XTA signal at time delay Δt_0 (shown in orange), while the scheme in Figs. 1(a) and 1(b) acquires only one such measurement. The increased statistics acquired at each pump-probe time delay make HRR-XMP useful for efficiently studying samples with small XTA signals.

AXMP collects XTA data at an adjustable set of pump-probe time delays in a single measurement. The acquired time delays are separated by δt, which can be as little as several ps. Thus, AXMP can efficiently capture sub-ns XTA sample dynamics, which are often of particular interest.[14–23] This is accomplished using a carefully selected pump laser repetition rate, which makes the acquired time delays increase by δt in each subsequent pump-probe cycle. For example, in Fig. 1(e), the orange dot on the far left represents XTA data acquired at a time delay Δt_0 after the first pump laser pulse, while the orange dots after the second and third laser pulses represent XTA data collected at time delays $\Delta t_0 + \delta t$ and $\Delta t_0 + 2\delta t$, respectively. The small spacing between the acquired pump-probe time delays measured by AXMP stands in contrast to HRR-XMP, in which XTA data are acquired at time delays separated by x-ray pulse spacing T_X (>10 ns).

The AXMP synchronization scheme is similar to laser-based Asynchronous Optical Sampling (ASOPS),[8,9,24–27] but it also introduces a new synchronization concept that increases the signal statistics measured at early pump-probe time delays. This is one of the main novel contributions of this work.

The rest of the paper is organized as follows: Sec. II describes the synchrotron beamline instrumentation and important practical aspects of the HRR-XMP and AXMP experiments. Section III shows the data acquired with HRR-XMP and AXMP and discusses the results. Section IV summarizes our contributions and future work.

The theory of AXMP synchronization and HRR-XMP are reported in Appendices B and C.

II. METHODS

A. Experimental setup

Figure 2 shows a schematic diagram of the experimental setup, which is used for both HRR-XMP and AXMP. The sample is delivered to the x-ray and laser beams in the form of a free-flowing liquid jet. A high repetition rate laser system (Duetto, Quanta Systems) is used to excite the sample and is shown in the blue box in Fig. 2. The Duetto laser system contains an oscillator and amplifier, which are synchronized with the probe x-ray pulses using two signals derived from the synchrotron RF clock. The oscillator synchronization signal (green arrow) is ~78.2 MHz and ensures the seed oscillator pulses are phase locked with the x-ray pulses. The amplifier trigger signal (orange arrow) has a widely variable frequency and determines the subset of amplified seed oscillator pulses. After the amplifier, the 1064 nm fundamental frequency of the laser can be doubled, tripled, or quadrupled to excite the sample. The details of the HRR laser system, x-ray and laser focusing and stabilization optics, and the high-speed sample jet can be found in March *et al.*[10]

The x-ray absorption spectra are measured using fluorescence detection and photon counting. The time-resolved sample fluorescence is measured by a pair of home-built avalanche photodiodes (APDs), which are shown in gray in the center of Fig. 2. These detectors produce fast voltage pulses (5 ns FWHM) in response to the absorption of x-ray photons. The detectors are connected via SMA cables to two Acqiris U5303A Analog to Digital Converter (ADC) cards, which are the main component of the XMP DAQ electronics (shown in the gray box in Fig. 2). The ADC cards time-tag the detector voltage pulses with respect to the ADC acquisition trigger (the purple arrow in Fig. 2) and accumulate the counts from many triggers into a histogram of photon arrival times. This histogram is used to calculate the XTA signal at many pump-probe time delays and one x-ray probe energy. The synchronization of the photon arrival time histogram bins (1.136 ns wide) is controlled by the acquisition sample clock (1760 MHz, yellow arrow in Fig. 2). We note that a total count rate of around 5×10^7 counts per second can be reliably obtained from each fluorescence detector. A brief description of the XTA data reduction procedure is given in Appendix A. The additional details of the XMP DAQ system (enclosed in the green box in Fig. 2) can be found in Kinigstein *et al.*[1]

The four electrical signals shown in Fig. 2 (oscillator synchronization signal, amplifier trigger signal, ADC acquisition trigger signal, and sampling clock signal) are all generated from the synchrotron RF clock (352 MHz), which ensures that the laser and data acquisition are synchronized with each other and with the x-ray pulses. The synchronization electronics used to generate these signals are represented by the dark green box in Fig. 2. These electronics can be reconfigured to accommodate the different synchronization schemes used by HRR-XMP and AXMP. The configuration of the synchronization electronics for HRR-XMP and AXMP is given in Appendices D and E, respectively.

B. High repetition rate x-ray multiprobe (HRR-XMP) data acquisition

HRR-XMP is a combination of XMP DAQ with HRR laser excitation. The goal of HRR-XMP is to increase the signal-to-noise ratio (SNR) of the XTA data surfaces acquired in an XMP DAQ histogram. The XTA spectra are still acquired at the time delays given by Eq. (2), but occur in a smaller time span determined by the laser repetition rate. To ensure that the time delays in each pump-probe cycle are identical, the time between laser pulses must be an integer multiple of the x-ray probe pulse spacing T_X as shown in Fig. 1(c). Many pump-probe cycles are acquired in each photon arrival time histogram, and the measurements at each time delay can, therefore, be averaged together to increase the SNR of the resulting XTA data surface. The time resolved sample fluorescence intensity is measured with nearly shot noise limited detection, which is shown in the supplementary material Sec. I.

In general, high repetition rate XTA experiments are subject to a number of important constraints,[10–13] and HRR-XMP is no different. HRR-XMP typically requires a high-speed sample jet to fully refresh the excited sample over the probe volume between adjacent laser pulses. This restricts the size of the pump and probe beams and

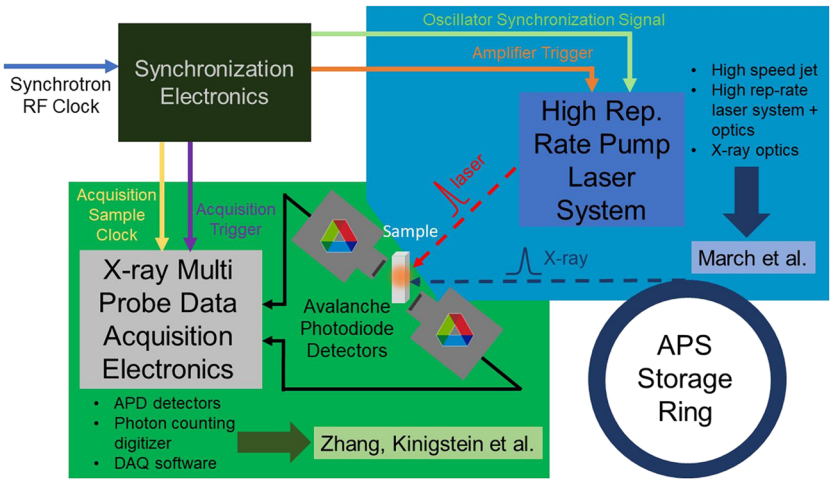

FIG. 2. Schematic of the hardware used in both the AXMP and HRR-XMP techniques. The details on X-ray Multiprobe data acquisition are reported by Kinigstein *et al.*[1] The details of High Repetition Rate XTA instrumentation are reported by March *et al.*[10]

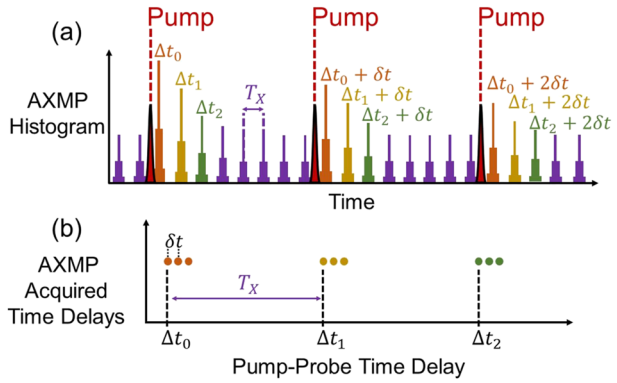

FIG. 3. Panel (a) shows a schematic photon arrival time histogram acquired using AXMP data acquisition. Panel (b) shows the pump-probe time delays where the XTA data are acquired.

requires active feedback to ensure their spatial stability.[10–13] Nevertheless, the advantage of acquiring low-noise XTA data at many time delays in a single measurement makes HRR-XMP a powerful technique for characterizing excited state phenomena in liquid-based samples.

C. Asynchronous x-ray multiprobe (AXMP) data acquisition

Many aspects of AXMP are similar to HRR-XMP. AXMP uses HRR laser excitation and measures the time resolved fluorescence using the XMP DAQ technique. However, AXMP uses a distinct synchronization scheme that enables acquisition of XTA data at time delays separated by only picoseconds. This makes AXPM ideal for characterizing XTA dynamics on the sub-ns time scale.

Figure 3(a) shows a schematic representation of a photon arrival time histogram acquired with AXMP. Each histogram contains many pump-probe cycles. The time delays in each cycle increase by δt (~5–10 ps) with respect to the previous. This requires a pump laser period that is δt less than an integer multiple of the x-ray pulse spacing T_X, as shown in Fig. 1(e). This effect enables AXMP to capture sub-ns XTA dynamics in a single histogram.

Figure 3(b) shows a diagram representing the set of pump-probe time delays acquired in an AXMP histogram. Each color-coded dot in Fig. 3(b) corresponds to a histogram peak in Fig. 3(a), and the position of the dot along the x-axis indicates the pump-probe time delay of that peak. For example, the first histogram peak after each laser pulse in Fig. 3(a) is colored orange. These peaks contain XTA data at pump-probe time delays indicated by the three orange dots on the left of Fig. 3(b). Likewise, the cluster of yellow dots in Fig. 3(b) comes from the second x-ray pulse after the laser in each pump-probe cycle. Because the x-ray pulses within each cycle are separated by T_X, each cluster of time delays in Fig. 3(b) is shifted by T_X with respect to the adjacent clusters. Since the time delays shift by δt in each subsequent pump-probe cycle, the dots within each cluster are separated by δt. In AXMP, the clusters of acquired time delays can be significantly shorter than the x-ray pulse spacing T_X, which results in XTA data acquired at an inhomogeneous distribution of pump-probe time delays. Furthermore, choosing a cluster width of, for example, $T_X/8$ results in 8× more XTA signal statistics accumulated at each pump-probe time delay compared to an AXMP acquisition with a cluster width of T_X (a fully homogeneous distribution of acquired time delays). This increase in statistics represents a novel aspect of the AXMP synchronization concept that distinguishes it from ASOPS synchronization and is explained in detail in Appendices B and C. The clustered distribution of acquired time delays and the resulting increase in signal statistics make AXMP useful for studying ns and sub-ns photoinduced sample dynamics. In such cases, the clusters of time delays are well suited to measure the fast spectral changes in the immediate vicinity of the laser pulse.

Several important parameters of the AXMP acquisition scheme are tunable, so they can be optimized to measure dynamics with different characteristic time scales. For example, the spacing between acquired spectra (δt) is determined by the oscillator frequency, which can be adjusted as desired. The time between laser pump pulses can be adjusted with the laser amplifier trigger. In the current implementation of AXMP, the width of the clusters can be varied in integer multiples of $T_X/8$.

III. RESULTS AND DISCUSSION

A. HRR-XMP

In this section, we demonstrate the capabilities of HRR-XMP by measuring the Fe K-edge XTA of a 50 mM aqueous $[Fe^{(II)}(CN)_6]^{4-}$ solution excited by the fourth harmonic (266 nm) of the fundamental output of the Duetto laser system. The pump laser frequency was 751.9 kHz corresponding to a laser period of ~1.33 μs. This results in a pump-probe cycle containing exactly 117 x-ray probe pulses mutually separated by T_X = 11.36 ns, giving 117 unique pump-probe time delays. One single data acquisition histogram contains ~169 000 time bins (each 1.136 ns wide) and a total of 145 pump-probe cycles. A histogram was acquired for each of the 289 probe energy points in the spectrum. After averaging the data from each pump-probe cycle, the final HRR-XMP data surface can be represented as a matrix containing 289 rows and 117 columns. The displayed data in Fig. 4 are the average of 22 HRR-XMP data surfaces collected over 9 h.

Panel Fig. 4(a) shows the XTA spectra generated by three selected x-ray bunches after the laser. Photoexcitation of $[Fe(CN)_6]^{4-}$ produces an oxidized ($[Fe^{(III)}(CN)_6]^{3-}$) species and an aquated ($[Fe^{(II)}(CN)_5H_2O]^{3-}$) species,[28–30] both of which contribute to the XTA spectrum measured at 100 ps [blue line in panel Fig. 4(a)]. The photo-oxidized species is known to quickly regenerate the ground state $[Fe^{(II)}(CN)_6]^{4-}$ molecule.[30,31] Thus, the spectra collected at later pump-probe time delays (greater than 11.36 ns) mostly reflect the spectrum of the photoaquated species [for example, the orange and green lines in Fig. 4(a)]. This situation is also shown in the full HRR-XMP data surface in Fig. 4(b). The spectra evolve smoothly at time delays greater than 11.37 ns, but there is a clear discontinuity between the first and second spectra after the laser. This apparent discontinuity reflects the unobserved decay dynamics of the photooxidized species that occur between the first two x-ray probe pulses after the laser.

Figure 4(c) shows the average of 20 XTA spectra acquired between 22 and 250 ns after the laser. The data in Fig. 4(c)

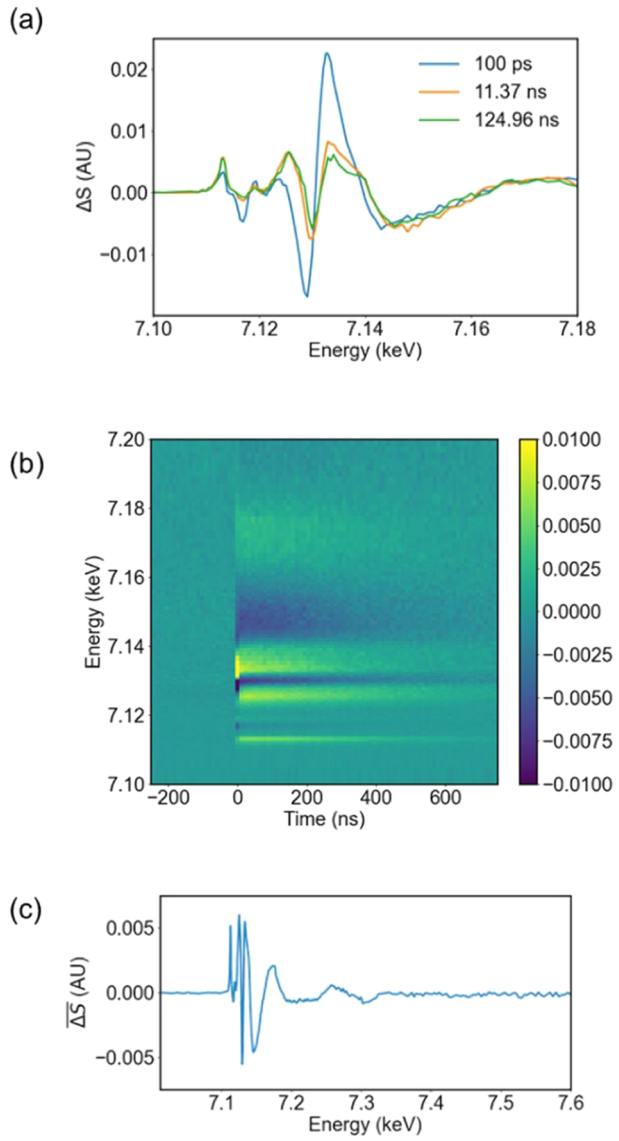

FIG. 4. Fe K-edge XTA data of 50 mM $[Fe^{(II)}CN_6]^{4-}$ in H_2O (excited at 266 nm) acquired with HRR-XMP. Panel (a) shows the XTA spectra generated by three x-ray bunches after the laser pulse. Panel (b) shows the XTA data surface. Panel (c) shows the average of 20 XTA spectra obtained between 22 and 250 ns after the laser pulse and displayed over the full range of the acquired probe.

are extracted from the data surface in Fig. 4(b). The highly efficient collection of XTA kinetic data with HRR-XMP histograms allows the spectrum to be measured over a relatively large probe energy range. For example, the data in Fig. 4 were acquired over a range of 650 eV, allowing structural and electronic information about the photoexcited species to be obtained through a combined analysis of the X-ray Absorption Near Edge Structure (XANES) and the Extended X-ray Absorption Fine Structure (EXAFS).

Thus, Fig. 4 illustrates both the strengths and limitations of HRR-XMP for measuring photochemical processes with XTA spectroscopy. The strength of HRR-XMP lies in the large amount of highly self-consistent XTA data obtained with a large signal-to-noise ratio. For example, the full XTA spectrum of $[Fe(CN)_6]^{4-}$ was acquired at 117 different pump-probe time delays and 289 energy points. Therefore, HRR-XMP provides an efficient way to characterize photochemical reaction dynamics on long-time scales ($>T_X$) with XTA spectroscopy. However, the XTA data are obtained at pump-probe time delays separated by T_X (in this case, 11.36 ns), which represents a limitation of the technique. In Sec. III B, we demonstrate AXMP data acquisition, which acquires XTA spectra at a set of time delays separated by just picoseconds.

B. AXMP

We demonstrate AXMP data acquisition by measuring the XTA dynamics of a 15 mM aqueous $[Fe(bpy)_3]^{2+}Cl_2$ (bpy: 2,2′-bipyridine) solution. The third harmonic of the Duetto laser system (355 nm, 10 ps FWHM) was used to excite the sample jet at ~1.95 MHz. The AXMP histogram contains 217 complete pump-probe cycles, with each cycle containing 45 x-ray probe pulses. This synchronization scheme acquired data in 45 clusters of pump-probe time delays separated by T_X. Each cluster was 1.42 ns ($=T_X/8$) wide and contained 217 time delays that were mutually separated by 6.5 ps. Figure 5(a) shows the XTA data surface obtained from the cluster of time delays closest to the laser pulse. The data from the 44 subsequent clusters of time delays and additional information about the experimental setup are given in the supplementary material Sec. II. Notably, the 217 time delays are a natural consequence of AXMP synchronization and were not obtained by physically changing the laser timing. Each scan of the beamline monochromator measures the complete XTA spectrum at ~9 700 time delays and 241 energy points and requires about 32 min to acquire (with an integration time of 6 s at each energy point). The data presented in this section are the average of 20 scans or ~11 h of signal integration.

Laser excitation of $[Fe^{II}(bpy)_3]^{2+}$ at 355 nm creates a metal-to-ligand charge transfer state (MLCT) with a singlet character.[32] The initially excited state relaxes to a high spin quintet on a sub 100 fs time scale, featuring significantly (~10%) increased bond lengths.[32–36] Representative XTA spectra obtained at time delays near the laser are shown in Fig. 5(b). The ultrafast relaxation from the singlet state makes the high-spin quintet the only significant species in these spectra, as reflected by the four isosbestic points at 7.131, 7.155, 7.180, and 7.216 keV. The weak oscillations in the XTA spectrum occurring below 7.12 keV result from the Fe 1s → 3d quadrupole transitions, which reflect changes in the electronic structure and orbital occupancy between the quintet excited state and low spin ground state.[33–37] Large photoinduced changes are observed with maxima at ~7.124 and ~7.164 keV and minima at ~7.144 and ~7.202 keV. These features result from changes in the 1s → 4p dipole transitions and are attributed to a combination of electronic and structural effects in the excited state.[33–37] The spectral dynamics shown in Figs. 5(a) and 5(b) illustrate the highly self-consistent XTA data obtained with AXMP.

Figure 5(c) shows the kinetics of the XTA spectrum ($\overline{\Delta S}$, blue dots) averaged over the large feature between 7.12 and 7.13 keV [this

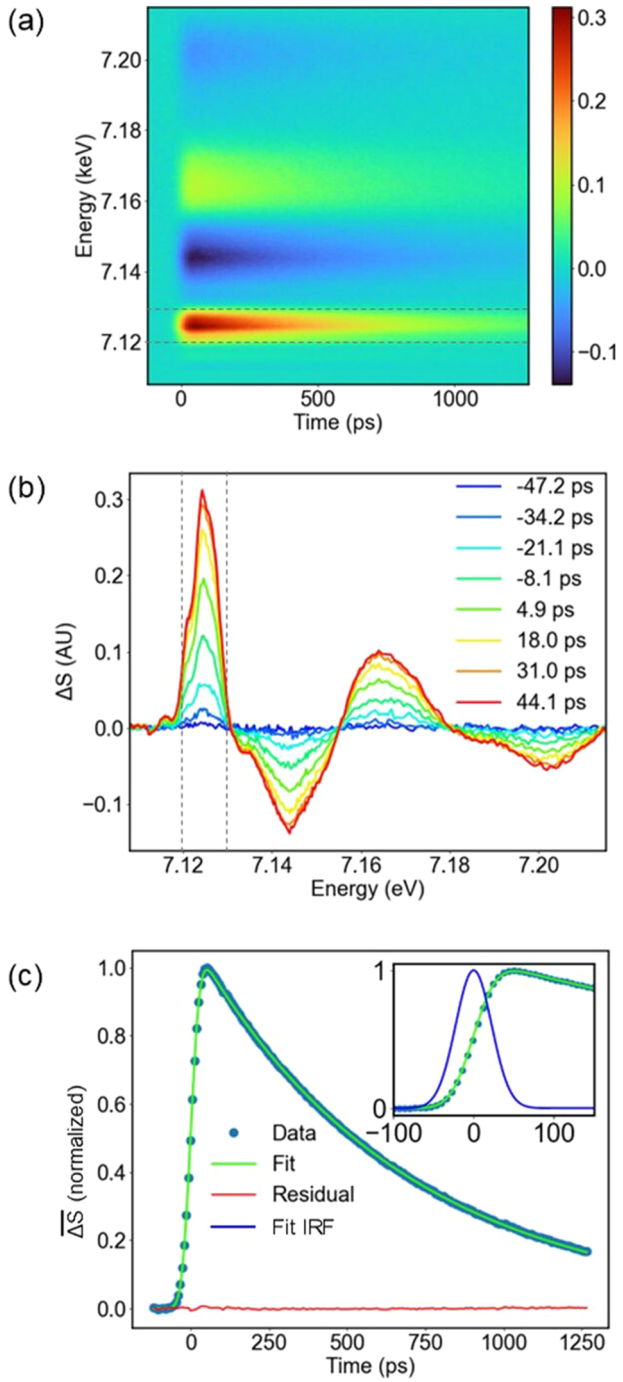

FIG. 5. Fe K-edge XTA data of 15 mM $[Fe^{(II)}(bpy)_3]^{2+}$ in H_2O (excited at 355 nm) acquired with AXMP. Panel (a) shows the XTA data surface from the first x-ray probe pulse after each laser pulse in the acquisition. Panel (b) shows the XTA spectra at a set of early time delays. The spectra in panel (b) are extracted from the data surface in panel (a). Panel (c) shows the normalized XTA kinetics averaged over the region between 7.12 and 7.13 keV [indicated by dotted lines in panels (a) and (b)], as well as a fit of this data and the residual of the fit. The inset in panel (c) shows the same kinetics at early times, along with the normalized fit instrument response function.

region is indicated by dotted lines in panels Figs. 5(a) and 5(b)]. The data in Fig. 5(c) are fit (green line) by a function of the form,

$$y = A\theta(t)e^{-t/\tau} \otimes \frac{e^{-t^2/2\sigma^2}}{\sigma\sqrt{2\pi}}. \quad (3)$$

Here, $A\theta(t)e^{-t/\tau}$ represents the expected concentration dynamics of the excited $[Fe^{II}(bpy)_3]^{2+}$ quintet species generated instantaneously by a laser pulse at $t = 0$. $\theta(t)$ is the Heaviside step function. In the fit model [Eq. (3)], this signal is convolved with a Gaussian instrument response function (IRF). The residual of the fit is shown by the red line in Fig. 5(c), and further details of the fitting procedure are reported in the supplementary material Sec. III. The extracted IRF is shown by the blue line in Fig. 5(c). The extracted IRF standard deviation (σ = 22.39 ± 0.06 ps) quantitatively agrees with the expected value of 22.4 ps, which is dominated by the width of the x-ray pulse (σ_X = 22 ps) and has a smaller contribution from the width of the laser pulse (σ_{Laser} = 4.25 ps). The extracted quintet decay time (τ = 671.9 ± 0.5 ps) of $Fe^{(II)}(bpy)_3$ in H_2O quantitatively agrees with some previous reports,[34,37] while it is slightly longer than others.[35,36] The small uncertainty of 0.5 ps in the decay lifetime, the quantitative agreement with the expected value of the IRF width, and the low fit residual are consequences of the high data quality obtained with the AXMP technique. In summary, Fig. 5 illustrates the strength of the AXMP technique in measuring sub-ns XTA dynamics.

IV. CONCLUSION

We have developed two novel data acquisition techniques for XTA spectroscopy: High Repetition Rate X-ray Multiprobe (HRR-XMP) and Asynchronous X-ray Multiprobe (AXMP). Both techniques use X-ray Multiprobe data acquisition (XMP DAQ) in combination with high repetition rate laser excitation. XMP DAQ rapidly cycles through XTA measurements at a large number of pump-probe time delays, which results in highly self-consistent XTA kinetics data. The high repetition rate laser used by HRR-XMP and AXMP can greatly improve the measured statistics, but it also necessarily limits the overall range of time delays. The high data collection efficiency of HRR-XMP makes it suitable for studying small XTA dynamic signals on a time scale of tens of ns. AXMP uses a novel synchronization scheme to acquire XTA data at time delays separated by only several ps, making it powerful for measuring photoexcited sample dynamics on ns and sub-ns time scales.

The data collection efficiency of HRR-XMP was demonstrated by measuring the complete Fe K-edge XTA spectrum of $Fe^{(II)}[CN]_6$ over an energy range of 650 eV and at 117 pump-probe time delays (mutually separated by 11.36 ns). Thus, HRR-XMP enables the study of photoexcited species through a combined analysis of the X-ray Absorption Near Edge Structure and Extended X-ray Absorption Fine Structure. The capabilities of AXMP were demonstrated by measuring the complete Fe K-edge XTA spectrum of $Fe^{(II)}[bpy]_3$ at a set of pump-probe time delays separated by only 6.5 ps (δt). The acquired spectra are obtained in clusters of time delays that are 1.42 ns wide and separated by 9.94 ns. The inhomogeneous distribution of acquired time delays significantly increased the achievable signal statistics, which is a consequence of the novel AXMP synchronization concept. Both δt and the cluster width

can be optimized to match the dynamic timescales of individual photoexcited samples.

Given the flexibility of AXMP synchronization and its suitability to measure sub-ns dynamics, we expect it to find useful applications in high repetition rate x-ray free-electron laser facilities. Combining AXMP synchronization with various data acquisition techniques (e.g., Timepix[38,39] readout) could yield a new generation of precision x-ray spectroscopy and scattering techniques for studying time-resolved processes. Finally, the highly self-consistent spectral dynamics acquired with HRR-XMP and AXMP present new challenges and opportunities for computational data analysis. We are currently working on statistical techniques to quantitatively extract kinetic information about photochemical reaction dynamics from the AXMP and HRR-XMP data surfaces. We expect that augmenting the tunability of AXMP and HRR-XMP with advanced data analysis techniques will enable an understanding of photochemical and photophysical processes in unprecedented detail.

SUPPLEMENTARY MATERIAL

supplementary material is available. This document contains an analysis of the noise acquired in XMP DAQ histograms, additional data acquired with AXMP on $[Fe^{II}(bpy)_3]^{2+}$, information about the fitting procedure used for the $[Fe^{II}(bpy)_3]^{2+}$ kinetics data, and additional details about the synchronization procedure.

ACKNOWLEDGMENTS

This work was supported by the Laboratory Directed Research and Development (LDRD) funding from the Argonne National Laboratory, provided by the Director, Office of Science, of the U.S. Department of Energy under Contract No. DE-AC02-06CH11357. The authors and users of the Advanced Photon Source at the Argonne National Laboratory acknowledge the U.S. Department of Energy, Office of Science, Office of Basic Energy Sciences, under Contract No. DE-AC02-06CH11357. C. Otolski, G. Doumy, and A. M. March also acknowledge the Department of Energy, Office of Science, Basic Energy Science, Chemical Sciences, Geosciences and Biosciences Division under Contract No. DE-AC02-06CH11357.

AUTHOR DECLARATIONS

Conflict of Interest

The authors have no conflicts to disclose.

Author Contributions

Eli Diego Kinigstein: Conceptualization (equal); Data curation (equal); Formal analysis (equal); Investigation (equal); Methodology (equal); Writing – original draft (equal); Writing – review & editing (equal). **Christopher Otolski**: Investigation (equal); Writing – review & editing (equal). **Guy Jennings**: Software (lead); Writing – review & editing (equal). **Gilles Doumy**: Investigation (equal); Writing – review & editing (equal). **Donald A. Walko**: Investigation (equal); Writing – review & editing (equal). **Xiaobing Zuo**: Formal analysis (equal); Funding acquisition (equal); Writing – review & editing (equal). **Jinghua Guo**: Funding acquisition (equal); Writing – review & editing (equal). **Anne Marie March**: Funding acquisition (equal); Investigation (equal); Writing – review & editing (equal). **Xiaoyi Zhang**: Conceptualization (lead); Data curation (lead); Formal analysis (equal); Funding acquisition (lead); Investigation (equal); Methodology (lead); Project administration (lead); Resources (lead); Supervision (lead); Writing – original draft (equal); Writing – review & editing (equal).

DATA AVAILABILITY

The data that support the findings of this study are available from the corresponding authors upon reasonable request.

APPENDIX A: PHOTON ARRIVAL TIME HISTOGRAMS AND XTA DATA REDUCTION

The following is a brief explanation of how the XTA signal is acquired at thousands of pump-probe time delays in a single measurement. We refer to this method of detecting time resolved x-ray fluorescence as XMP DAQ. The data reduction procedure that converts the photon arrival time histogram (generated by the Acqiris ADCs described in Sec. II A) to the XTA data surface is almost identical for HRR-XMP and AXMP and is performed using a software developed in-house called QAVRG (http://qavrg.sourceforge.net/). QAVRG also communicates with the ADCs to configure the acquisition.

A schematic photon arrival time histogram is shown in Fig. 6(a). Histograms are acquired for each desired energy point in the XTA spectrum. The probe energy is selected with the beamline monochromator, and the ADC accumulates time-tagged sample fluorescence counts in the histogram for roughly 4 s. Synchronization between the ADC acquisition trigger and the x-ray pulses forces the histogram to take on a peaked structure, which reflects the pulsed synchrotron radiation. The time between the histogram peaks corresponds to the x-ray pulse spacing T_X, and one peak appears for each x-ray pulse in the pump-probe cycle. A direct correspondence exists between the color-coded histogram peaks in Fig. 6(a) and the x-ray pulses in Fig. 1(b). The laser pump pulse [the red peak indicated in Fig. 6(a)] is synchronized with both the ADC acquisition trigger and the x-ray pulses. Thus, the total counts in each histogram peak are proportional to the x-ray fluorescence intensity of the sample at a corresponding set of well-defined time delays from the laser pump pulse [given by Eq. (2)]. The pump-probe time delays of the first three histogram peaks after the laser are indicated by text in Fig. 6(a). To calculate the time resolved f-XAS dynamics [Fig. 6(b)] from the histogram in Fig. 6(a), the counts within each peak are summed together and then normalized by a signal proportional to the incident flux.

The f-XAS signal before (and long-after) the laser pulse in Fig. 6(b) represents the ground state f-XAS of the sample at the incident x-ray probe energy. The increase in measured fluorescence counts following the laser pulse in Figs. 6(a) and 6(b) results from the creation of a photoexcited species. In this example, the photoexcited species has a larger f-XAS signal at the probe energy. The subsequent decrease in this signal reflects the decrease in the photoexcited species concentration as it decays back to the ground state. The resulting XTA dynamics are shown in Fig. 6(c), which are

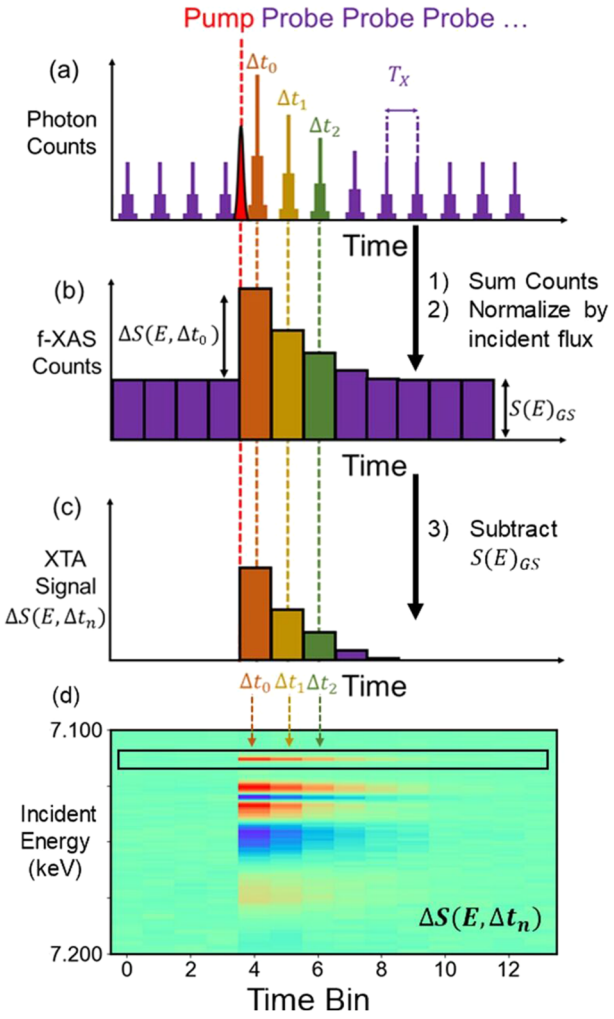

FIG. 6. A schematic illustrating the data reduction steps that calculate the XTA data surface from the acquired time resolved histogram. Panel (a) shows a photon arrival time histogram, with the red laser pump pulse overlaid for clarity. Panel (b) shows the time resolved fluorescence detected XAS (f-XAS) dynamics at one probe energy and indicates the steps used to calculate it from the data in panel (a). Panel (c) shows the XTA dynamics at one probe energy calculated from panel (b). Panel (d) shows the XTA data surface, which is assembled from a collection of XTA dynamic signals [panel (c)] acquired at different probe energies.

calculated by subtracting the sample's ground state f-XAS $[S(E)_{GS}]$ from its excited state f-XAS $[S(E, \Delta t_n)]$. Finally, the full XTA data surface in Fig. 6(d) is assembled from the XTA dynamics [Fig. 6(c)] acquired at each probe energy. We note that a 4-s measurement at each probe energy is usually insufficient to obtain enough probe statistics for a high-quality XTA dataset. Therefore, it is common practice to measure all energy points in the XTA spectrum 10–20 times and average the resulting data surfaces together.

In summary, Fig. 6 illustrates the main steps of how XMP DAQ acquires the XTA signal at many time delays in a single measurement. The XMP histogram effectively cycles through the measurements at each time delay so that all data are acquired under the identical average experimental conditions. Both HRR-XMP and AXMP use photon arrival time histograms to acquire time resolved fluorescence data and take advantage of the high-quality XTA dynamics produced by this technique.

APPENDIX B: AXMP AND HRR-XMP: LASER OSCILLATOR SYNCHRONIZATION SIGNAL AND DATA ACQUISITION TRIGGER RATE

An AXMP acquisition requires four properly synchronized signals shown in Fig. 2: (1) the laser oscillator synchronization signal (green line), (2) the amplifier trigger signal (orange line), (3) the ADC acquisition trigger (purple line), and (4) the acquisition sampling clock (yellow line). Together, these signals determine important characteristics of the AXMP acquisition, such as the spacing between the acquired spectra δt and the width of the clusters of acquired time delays (shown in Fig. 3). A self-consistent synchronization scheme requires a specific relationship between the frequencies of signals (1) and (3), as well as a specific form of signal (2). The required relationship between these signals follows from examining the non-trivial beating pattern between the pump laser oscillator (at frequency $\tilde{\omega}_O = \omega_O + \delta\omega$) and the x-ray pulses (at frequency $\omega_x = 9\omega_O/8$).

In synchrotron-based XTA measurements, the pump laser oscillator is synchronized to the probe x-ray pulses by locking its repetition rate to a sub-harmonic of the synchrotron RF signal. At the APS, the synchrotron RF signal is at 352 MHz (ω_{RF}), and the x-ray probe pulses occur at a repetition rate $\omega_X = \omega_{RF}/4 = 88$ MHz (characteristic of APS 324 bunch mode). Typically, the laser oscillator is locked to a signal at $\omega_O = \omega_{RF}/4.5 = 78.22$ MHz[10] (for example, in HRR-XMP). However, in AXMP, the oscillator is locked to a frequency $\tilde{\omega}_O$ that is slightly (~1 kHz) different from ω_O but is still derived from the synchrotron RF signal. We define

$$\tilde{\omega}_O = \omega_O + \delta\omega = \omega_O\left(1 + \frac{1}{L}\right), \tag{B1}$$

where L is a large integer, typically around 10^5. The laser oscillator remains phase locked with the x-ray pulse train, but with a non-trivial beating pattern occurring between the oscillator (at $\tilde{\omega}_O = \omega_O + \delta\omega$) and the x-ray probe pulses (at $\omega_X = 8\omega_O/9$).

In previous laser-based applications[8,9,24–27,40–43] of asynchronous sampling, the pump-probe time delay increases with each subsequent pump probe cycle due to a frequency mismatch between the pump and probe. However, the time delay wraps around to its original value at the beat frequency between the pump and probe ($\omega_{beat} = \delta\omega = \omega_{pump} - \omega_{probe}$). Triggering the data acquisition electronics (for example, an oscilloscope) at ω_{beat} enables the probe signal to be accumulated over many beating cycles and averaged to obtain sufficient statistics. Thus, the highest value of the data acquisition trigger rate (Γ_{exp}) is equal to the beat frequency ω_{beat} ($=\delta\omega \sim 1$ kHz), which strongly limits the rate that signal statistics can be acquired at each pump-probe time delay. The novelty and enhanced functionality of the AXMP synchronization concept result from the different set of beat frequencies that occur between the laser oscillator (at frequency $\tilde{\omega}_O = \omega_O + \delta\omega$) and the x-ray probe pulses (at frequency $\omega_X = 9\omega_O/8$). These beat frequencies are given by $\omega_{beat} = 9\delta\omega/m$ (where m is an integer) and enable the AXMP data acquisition trigger rate Γ_{exp} to be up to nine times higher than the

oscillator detuning frequency $\delta\omega$. Triggering the DAQ at a beat frequency of $9\delta\omega/m$ results in the "clustered" distribution of acquired time delays in Fig. 3, with a cluster width given by $mT_X/8$.

The possible values of ω_{beat} and the experimental repetition Γ_{exp} rate in AXMP are derived from two conditions. First, we require an integer number (J_O) of oscillator periods $\tilde{T}_O$ (=$1/\tilde{\omega}_O$) in the time period between DAQ triggers T_A (=$1/\Gamma_{exp}$). Using Eq. (B1), we have

$$T_A = J_O\tilde{T}_O = J_O\frac{L}{\omega_O(L+1)}. \tag{B2}$$

If Eq. (B2) is not satisfied, f-XAS counts from different pump-probe time delays will be mixed together in each histogram peak. Next, the time period between DAQ triggers is also required to be an integer (J_X) multiple of the x-ray pulse period T_X (=$1/\omega_X$),

$$T_A = J_X T_X = J_X\frac{8}{9\omega_O}. \tag{B3}$$

This condition ensures that each x-ray pulse has a fixed location in the histogram. If Eq. (B3) is not satisfied, the spacing between the histogram peaks will no longer be equal to T_X. Combining Eqs. (B2) and (B3), we obtain

$$\frac{8J_X}{L} = \frac{9J_o}{(L+1)}. \tag{B4}$$

Equation (B4) is a polynomial that must be satisfied with integer values (L, J_X, and J_O) for an AXMP acquisition. Each solution corresponds to a distinct beat frequency between the laser oscillator and the x-ray probe pulses and, therefore, corresponds to a different experimental repetition rate Γ_{exp} (=$1/T_A$), which can be deduced from Eq. (B2) or Eq. (B3). This type of polynomial is called a Diophantine equation because only integer solutions are of interest. We assume solutions of the form

$$J_O = \frac{m(L+1)}{9}, \tag{B5a}$$

$$J_X = \frac{mL}{8}, \tag{B5b}$$

where m is an integer introduced to capture a larger set of solutions to Eq. (B5). While there may be more solutions to Eq. (B4) than those that follow from the assumptions in Eqs. (B5a) and (B5b), but they are not of present interest. Clearly, only specific values of L can satisfy Eqs. (B5a) and (B5b) simultaneously.

The solutions for L are given by

$$L = 8 + 72x, \tag{B6}$$

where x is any integer greater than zero. The combination of Eqs. (B5a), (B5b), and (B6) represent a family of solutions (L, J_X, and J_O) to Eq. (B4) in terms of two integers (m and x), as can be explicitly verified. Thus, given the values of m and x, we can define two of the three important signals for an AXMP acquisition. Usable oscillator locking signal frequencies ($\tilde{\omega}_O$) are given from Eqs. (B6) and (B1), and the corresponding data acquisition trigger rates ($\Gamma_{exp} = 1/T_A$) are given by Eqs. (B5b) and (B3). Thus, this discussion defines the constraints on two out of the four necessary signals for an AXMP acquisition. We note that the oscillator synchronization signal frequency in HRR-XMP is simply $\omega_O = \omega_{RF}/4.5 = 78.22$ MHz. While there is a lot of freedom in choosing the data acquisition trigger rate in HRR-XMP, some important considerations about this choice are given in the supplementary material Sec. IV.

APPENDIX C: AXMP AND HRR-XMP: LASER AMPLIFIER SYNCHRONIZATION

We now examine the behavior of the laser amplifier trigger in AXMP and HRR-XMP, which determines the structure of the laser pump-pulse train and is the final synchronization signal from Fig. 2 that needs to be defined. The laser amplifier selects one out of every N oscillator pulses to amplify and excite the sample. The synchronization of the amplifier trigger determines both N and which subset of oscillator pulses is selected. Figure 7 illustrates the synchronization between the x-ray probe pulses (blue arrows) and the oscillator pulses in the case of HRR-XMP (red arrows) and AXMP (green arrows). In this example, one out of every eight oscillator pulses is amplified (N = 8), which is indicated by the three pink boxes. Comparing the blue x-ray pulses with the red oscillator pulses (HRR-XMP) shows that the frequency difference between them causes the delay between each subsequent pair of pulses to increase. However, their relative frequencies ($\omega_X = 9\omega_O/8$) imply that the same time delay is recovered after every eight oscillator pulses (nine x-ray pulses). Thus, Figs. 7(a) and 7(b) illustrate that in HRR-XMP, N must be a multiple of 8, and this condition ensures that the same set of pump-probe time delays are obtained for every pump pulse. The amplifier trigger frequency is, therefore, defined as ω_O/N in HRR-XMP, where N is any multiple of 8 greater than 8.

In AXMP, the oscillator is locked to a signal at $\tilde{\omega}_O = \omega_O(1 + 1/L)$ (green arrows in Fig. 7), which causes the delay between the oscillator pulses and the signal at frequency ω_O to increase by

$$\widetilde{\delta t} = T_O - \tilde{T}_O = \frac{1}{(L+1)\omega_O} \tag{C1}$$

in each subsequent period. This situation is indicated by the increasing time delay between the green and red arrows from left to right in Fig. 7. After N oscillator pulses, the accumulated time delay is $\delta t = N\widetilde{\delta t}$. Figure 7 shows that if N is selected to be a multiple of 8 in AXMP, the time delay between the amplified pump pulse (green arrows in pink boxes) and the probe x-ray pulses will also increase by δt in each pump-probe cycle. For example, the time delay of the green pump pulses on the left of the figure is zero (as indicated by its vertical alignment with the blue arrows), but the time delays of the second and third pump pulses are increased by δt and $2\delta t$, respectively.

The shift in pump-probe time delays illustrated in Fig. 7 continues to accumulate in steps of $\widetilde{\delta t}$ for each of the J_O oscillator pulses [defined in Eq. (B5a)] during the acquisition. Thus, in the time period between DAQ triggers (T_A), the pump laser will accumulate a total delay with respect to the x-ray probe pulses of

$$\Delta\tau = J_O\widetilde{\delta t} = m\frac{T_X}{8} = m(1.42\text{ ns}). \tag{C2}$$

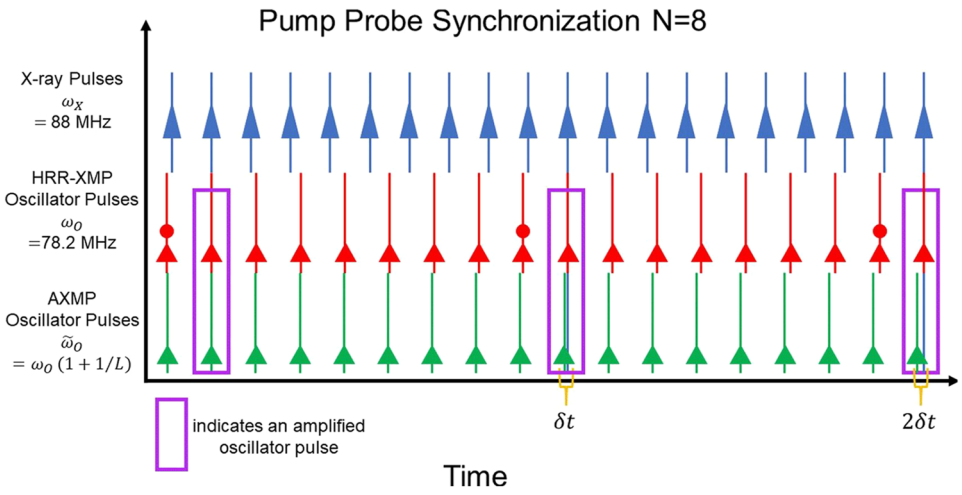

FIG. 7. An exemplary illustration of the synchronization between the x-ray pulses (blue arrows, top row) and the seed oscillator pulses in HRR-XMP synchronization (red arrows, middle row) and the seed oscillator pulses in AXMP synchronization (green arrows, bottom row). The pink boxes indicate the oscillator pulses amplified to excite the sample. In this case, one out of every eight oscillator pulses is amplified, thus N = 8.

By definition, $\Delta\tau$ is also equal to the width of the clusters of acquired pump-probe time delays shown in Fig. 3. Equation (C2) says the width of these clusters has a minimal value of $T_X/8$ (1.42 ns) and is proportional to m. Previous laser-based asynchronous acquisition techniques most closely resemble the case $m = 8$ because this corresponds to $\Delta\tau = T_X$ and results in a homogeneous distribution of acquired time delays (no clusters).

The experimental repetition rate Γ_{exp} is the inverse of the time period between DAQ triggers. Note that for each DAQ trigger, only one fluorescence photon can be added to each pump-probe time delay in the histogram. Thus, Γ_{exp} determines how quickly statistics can be accumulated at each time delay and is given by

$$\Gamma_{\text{exp}} = \frac{1}{T_A} = \frac{9\delta\omega}{m}, \tag{C3}$$

which can be derived based on Eqs. (B5b), (B3), and (B1). Equations (C2) and (C3) show that selecting $m > 1$ both increases the width of the acquired clusters and proportionally decreases the repetition rate. Thus, limiting the clusters to 1.42 ns ($m = 1$) enables the accumulation of experimental statistics eight times faster than the case of a homogeneous distribution of time delays ($m = 8$). This makes the AXMP synchronization concept useful for studying sub-ns dynamics, in which we are mostly interested in time delays immediately after the laser. Importantly, the possibility to obtain a synchronization scheme with $m < 8$ results from the expanded set of beat frequencies between $\tilde{\omega}_O$ and ω_X. However, implementing such a scheme imposes stringent requirements on the form of the amplifier trigger signal and the resulting pump pulse train.

Figure 7 illustrates that the number of oscillator pulses in each pump-probe cycle (N) must be a multiple of 8, while Eq. (B5a) places a constraint on the total number of oscillator pulses in an acquisition. Combining these two conditions illustrates the necessary requirements for the pump laser pulse train. This situation is shown in Fig. 8. Panel (a) shows the acquisition trigger period (T_A), which is required to be an integer (J_O) multiple of the oscillator period ($\tilde{T}_O = 1/\tilde{\omega}_O$). The red lines in Fig. 8(b) represent the laser pump pulses during the acquisition period. Using the above definitions of J_O and L, the number of laser pulses (and the number of pump-probe cycles) in one acquisition can be written as

$$J_O/N = m(1 + 8x)/N, \tag{C4}$$

with x defined as an integer in Eq. (B6). While N must be a multiple of 8, the numerator of Eq. (C4) cannot be a multiple of 8 (in the case of $m < 8$). Thus, J_O/N cannot be an integer, which means that an integer number of pump-probe cycles cannot fit in an acquisition. This situation is illustrated in Fig. 8(b). The black arrows in Fig. 8(b) show that the first six pump pulses in the acquisition are mutually separated by N oscillator periods, and the green arrow indicates that the last pump pulse of each acquisition is separated from

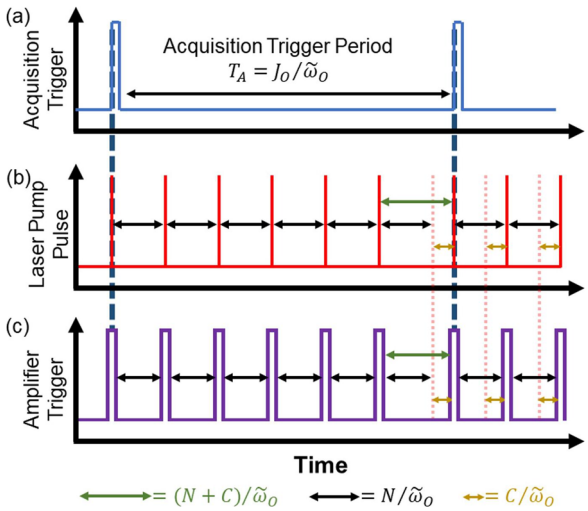

FIG. 8. Timing diagram illustrating the synchronization between the acquisition trigger [panel (a)], the pump laser pulse train [panel (b)], and the amplifier trigger [panel (c)].

the first pump pulse of the next acquisition by N + C oscillator periods. Figure 8(c) shows the amplifier trigger signal, which is necessary to create the laser pulse train in Fig. 8(b). The additional C oscillator periods at the end of the acquisition (yellow arrows) represent the non-integer part of Eq. (C4) and are necessary to conform with Eqs. (B2) and (B5a). They also make the pump laser pulse train (and the laser amplifier trigger) aperiodic. Only when $m = 8$ (or a multiple of 8) can Eq. (C4) result in an integer number of pump-probe cycles in an acquisition, and only in this case can the pump laser pulse train be fully periodic. Thus, Fig. 8 illustrates the required behavior of the amplifier trigger signal, which is the final signal required to configure an AXMP acquisition.

This completes the description of the AXMP synchronization concept. In summary, the non-trivial beating pattern between $\tilde{\omega}_O$ and ω_X enables AXMP acquisitions to be triggered at a faster rate and acquire more experimental statistics than in previous laser-based asynchronous acquisition concepts. However, obtaining the increased experimental repetition rate requires an aperiodic pump laser pulse train. The faster experimental repetition rate necessarily causes the acquired time delays to take on the clustered appearance shown in Fig. 3. These clusters of time delays make AXMP ideal for studying sub-ns dynamics using XTA. The data shown in Fig. 5 were obtained with L = 78 344, J_O = 8 705, J_X = 9 793, and N = 40. These values resulted in $\delta\omega \sim 1$ kHz, $\delta t \sim 6.5$ ps, and a DAQ trigger rate of ~9 kHz. Each AXMP histogram contained 217 pump-probe cycles; thus, each 1.42 ns cluster of time delays contained the XTA spectra measured at 217 time delays. The synchronization electronics (hardware) used to generate the four signals for HRR-XMP and AXMP are described in subsequent sections.

APPENDIX D: HRR-XMP SYNCHRONIZATION ELECTRONICS

Figure 9 shows the synchronization electronics required for an HRR-XMP acquisition. Note the correspondence of the color-coded lines representing the four synchronization signals in Fig. 2. The Duetto laser oscillator repetition rate is locked to a signal (the light green line in Figs. 2 and 9) at ω_O = 78.2 MHz, which is generated by dividing the synchrotron RF frequency (ω_{RF} = 352 MHz, blue in Fig. 2) by 4.5 with a homebuilt frequency divider. Fine adjustments

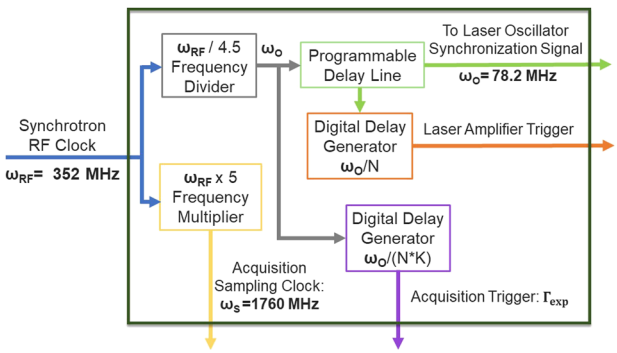

FIG. 9. Schematic representing the synchronization electronics used for an HRR-XMP acquisition.

of the pump-probe time delay (in 5 ps increments) are accomplished by modifying the phase of the oscillator synchronization signal with a Gigabaudics programable delay line (PADL3-5-12-15355, light green box in Fig. 9). Further details regarding the temporal (and spatial) pump-probe overlap (including in operational modes with larger values of T_X) are given in March *et al.*[10]

The Duetto regenerative amplifier selects one out of every N (where N is an integer greater than 12) oscillator seed pulses to amplify and excite the sample. The implemented value of N is determined by parameters supplied to the Duetto user interface and the frequency of the amplifier trigger signal. The amplifier trigger signal is generated by dividing the oscillator synchronization signal frequency by N using a Stanford Research Systems (SRS) DG 645 (orange box in Fig. 9). N is typically 40–780, yielding laser excitation pulses in a frequency range between 100 kHz and 2 MHz.

In HRR-XMP, the ADC acquisition trigger (purple line in Figs. 2 and 9) frequency Γ_{exp} must be an integer sub-multiple of the pump laser frequency, synchronized with the x-ray probe pulses, and independent of the pump-probe time delay (which is implemented with the Gigabaudics delay line). Thus,

$$\Gamma_{exp} = \frac{\omega_O}{NK}, \tag{D1}$$

where K is an integer equal to the number of pump-probe cycles in the time between the DAQ acquisition triggers T_A ($=1/\Gamma_{exp}$). The acquisition trigger is generated with a separate DG645 (purple box in Fig. 9) analogously to the amplifier trigger. K is often around 100, yielding Γ_{exp} = 10 kHz and an acquisition period T_A of around 100 μs.

The choice of K (together with the synchrotron storage ring operational mode) determines the number of x-ray pulses (J_X) in the acquisition period T_A. The relationship between J_X and the number of electron bunches in the synchrotron storage ring has an important impact on the quality of the acquired data. HRR-XMP and AXMP were deployed in APS 324 bunch mode, and in this case, optimal performance is obtained when J_X shares no common factors with 324. This issue is explained in detail in the supplementary material Sec. IV.

Finally, to ensure the consistency and quality of the acquired histogram, a sampling clock signal at frequency ω_S (1760 MHz) is supplied to the PCXMP data acquisition electronics (yellow line in Figs. 2 and 6); see Kinigstein *et al.* for details.

Thus, Fig. 9 shows how to configure the synchronization electronics for an HRR-XMP acquisition and describes how the four important signals (oscillator locking signal, amplifier trigger, DAQ acquisition trigger, and sampling clock signal) are generated for a consistently synchronized scheme.

APPENDIX E: AXMP SYNCHRONIZATION ELECTRONICS

Similar to HRR-XMP, the AXMP synchronization electronics (Fig. 10) generate four signals to lock the laser and acquisition to the x-ray pulses. The oscillator synchronization signal at frequency $\tilde{\omega}_O$ (light green line in Fig. 10) is generated by a frequency synthesizer (Windfreak Synth HD, light blue box in Fig. 10), which takes a signal at ω_O (gray line in Fig. 10) as the reference input. The frequency synthesizer effectively multiplies the reference ω_O signal frequency

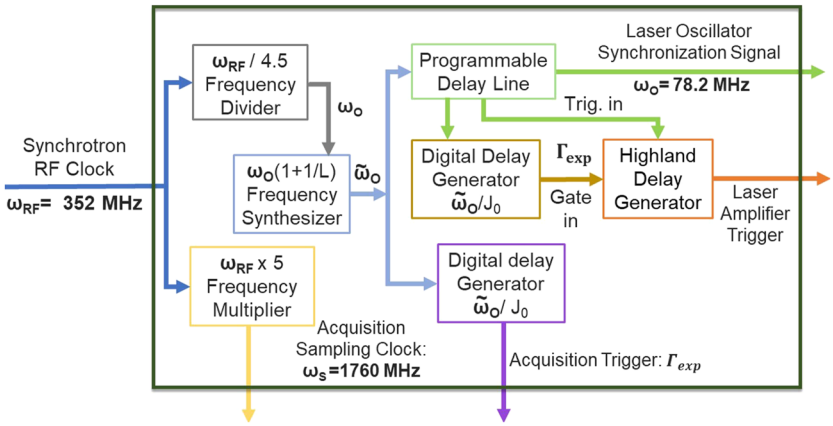

FIG. 10. Schematic representing the synchronization electronics used for an AXMP acquisition.

by $1 + 1/L \approx 1.000\,01$ and generates the $\tilde{\omega}_O$ signal with a phase noise of around −130 dBc/Hz at 1 kHz offset and 110 fs total jitter, which is sufficient quality to lock the Duetto oscillator. We note that $\delta\omega \sim 1$ kHz is within the locking bandwidth of many laser oscillators, including the Duetto. Thus, an oscillator configured to lock to frequency ω_O can usually also lock to $\tilde{\omega}_O$ without any changes to the hardware. This attractive aspect of AXMP means it can be implemented, reconfigured, and reversed with relative ease. Finally, the Gigabaudics unit (the light green box in Fig. 10) shifts the phase of the $\tilde{\omega}_O$ signal to enable a fine adjustment of the pump-probe time delay.

As described in Appendix B, the time period between acquisition triggers contains J_O seed oscillator pulses. Thus, the acquisition trigger (purple line in Fig. 10) is generated by dividing the (light blue) $\tilde{\omega}_O$ signal frequency by J_O with the DG645 (purple box in Fig. 10). Typically, Γ_{exp} is kept between 100 and 5 kHz. Similar to HRR-XMP, a sample clock signal at ω_S is supplied to the digitizer (yellow line in Fig. 10), which ensures the consistency and quality of the histogram.

The laser amplifier trigger signal [shown in Fig. 8(c)] is represented by the orange line in Fig. 10. This signal is generated by a Highland T564 digital delay generator (orange box in Fig. 10). The aperiodic amplifier trigger signal requires the T564 to operate in burst mode with an external gate. The oscillator synchronization signal at $\tilde{\omega}_O$ (light green line) is used as the external trigger for the T564. Burst mode is configured to count the number of external triggers and output one pulse to the laser amplifier for every N received. This effectively generates the equally spaced trigger pulses in the middle portion of Fig. 8(c). However, when the voltage on the T564 gate input (the gold line in Fig. 8) is high, the unit is blocked from receiving triggers, effectively pausing the burst mode counting electronics until the gate voltage decreases below the threshold. To generate the phase shift in the amplifier trigger signal shown in Figs. 8(c) and 8(a) gate pulse with a length of C oscillator periods is supplied to the T564 at the end of each acquisition. The gate signal is generated by a DG645 (gold box in Fig. 10). The Duetto regenerative amplifier can accommodate "on the fly" changes in the amplifier trigger phase and produces a close approximation to the laser pulse train in Fig. 8(b). Thus, Fig. 10 shows how to configure the synchronization electronics for an AXMP acquisition and describes how the four important signals (oscillator locking signal, amplifier trigger, DAQ acquisition trigger, and sampling clock signal) are generated for a consistently synchronized scheme. The novel aspects of this setup include locking the laser oscillator to a signal generated by a frequency synthesizer and the aperiodic laser amplifier trigger generated by the Highland delay generator.

REFERENCES

[1] E. D. Kinigstein, G. Jennings, C. A. Kurtz, A. M. March, X. Zuo, L. X. Chen, K. Attenkofer, and X. Zhang, Rev. Sci. Instrum. **92**, 085109 (2021).
[2] D. Moonshiram, C. Gimbert-Suriñach, A. Guda, A. Picon, C. S. Lehmann, X. Zhang, G. Doumy, A. M. March, J. Benet-Buchholz, A. Soldatov, A. Llobet, and S. H. Southworth, J. Am. Chem. Soc. **138**, 10586 (2016).
[3] D. Moonshiram, A. Guda, L. Kohler, A. Picon, S. Guda, C. S. Lehmann, X. Zhang, S. H. Southworth, and K. L. Mulfort, J. Phys. Chem. C **120**, 20049 (2016).
[4] Z.-J. Li, F. Zhan, H. Xiao, X. Zhang, Q.-Y. Kong, X.-B. Fan, W.-Q. Liu, M.-Y. Huang, C. Huang, Y.-J. Gao, X.-B. Li, Q.-Y. Meng, K. Feng, B. Chen, C.-H. Tung, H.-F. Zhao, Y. Tao, and L.-Z. Wu, J. Phys. Chem. Lett. **7**, 5253 (2016).
[5] Q. Kong, D. Khakhulin, I. A. Shkrob, J. H. Lee, X. Zhang, J. Kim, K. H. Kim, J. Jo, J. Kim, J. Kang, V.-T. Pham, G. Jennings, C. Kurtz, R. Spence, L. X. Chen, M. Wulff, and H. Ihee, Struct. Dyn. **6**, 064902 (2019).
[6] P. Gotico, D. Moonshiram, C. Liu, X. Zhang, R. Guillot, A. Quaranta, Z. Halime, W. Leibl, and A. Aukauloo, Chem. Eur. J. **26**, 2859 (2020).
[7] D. Moonshiram, A. Picón, A. Vazquez-Mayagoitia, X. Zhang, M.-F. Tu, P. Garrido-Barros, J.-P. Mahy, F. Avenier, and A. Aukauloo, Chem. Commun. **53**, 2725 (2017).
[8] A. Bartels, R. Cerna, C. Kistner, A. Thoma, F. Hudert, C. Janke, and T. Dekorsy, Rev. Sci. Instrum. **78**, 035107 (2007).
[9] R. Gebs, G. Klatt, C. Janke, T. Dekorsy, and A. Bartels, Opt. Express **18**, 5974 (2010).
[10] A. M. March, A. Stickrath, G. Doumy, E. P. Kanter, B. Krässig, S. H. Southworth, K. Attenkofer, C. A. Kurtz, L. X. Chen, and L. Young, Rev. Sci. Instrum. **82**, 073110 (2011).
[11] F. A. Lima, C. J. Milne, D. C. V. Amarasinghe, M. H. Rittmann-Frank, R. M. van der Veen, M. Reinhard, V.-T. Pham, S. Karlsson, S. L. Johnson, D. Grolimund, C. Borca, T. Huthwelker, M. Janousch, F. van Mourik, R. Abela, and M. Chergui, Rev. Sci. Instrum. **82**, 063111 (2011).
[12] A. Britz, T. A. Assefa, A. Galler, W. Gawelda, M. Diez, P. Zalden, D. Khakhulin, B. Fernandes, P. Gessler, H. Sotoudi Namin, A. Beckmann, M. Harder, H. Yavaş, and C. Bressler, J. Synchrotron Radiat. **23**, 1409 (2016).

[13]D. Göries, B. Dicke, P. Roedig, N. Stübe, J. Meyer, A. Galler, W. Gawelda, A. Britz, P. Geßler, H. Sotoudi Namin, A. Beckmann, M. Schlie, M. Warmer, M. Naumova, C. Bressler, M. Rübhausen, E. Weckert, and A. Meents, Rev. Sci. Instrum. **87**, 053116 (2016).
[14]A. Huijser, Q. Pan, D. van Duinen, M. G. Laursen, A. El Nahhas, P. Chabera, L. Freitag, L. González, Q. Kong, X. Zhang, K. Haldrup, W. R. Browne, G. Smolentsev, and J. Uhlig, J. Phys. Chem. A **122**, 6396 (2018).
[15]D. Hayes, R. G. Hadt, J. D. Emery, A. A. Cordones, A. B. F. Martinson, M. L. Shelby, K. A. Fransted, P. D. Dahlberg, J. Hong, X. Zhang, Q. Kong, R. W. Schoenlein, and L. X. Chen, Energy Environ. Sci. **9**, 3754 (2016).
[16]D. Hayes, L. Kohler, R. G. Hadt, X. Zhang, C. Liu, K. L. Mulfort, and L. X. Chen, Chem. Sci. **9**, 860 (2018).
[17]J. Nyakuchena, S. Ostresh, D. Streater, B. Pattengale, J. Neu, C. Fiankor, W. Hu, E. D. Kinigstein, J. Zhang, X. Zhang, C. A. Schmuttenmaer, and J. Huang, J. Am. Chem. Soc. **142**, 21050 (2020).
[18]B. Pattengale, Q. Liu, W. Hu, S. Yang, P. He, S. L. Tender, Y. Wang, X. Zhang, Z. Zhou, J. Zhang, and J. Huang, J. Phys. Chem. C **123**, 17994 (2019).
[19]J. Hong, T. J. Fauvell, W. Helweh, X. Zhang, and L. X. Chen, J. Photochem. Photobiol. Chem. **372**, 270 (2019).
[20]A. Hassan, X. Zhang, C. Liu, and P. T. Snee, J. Phys. Chem. C **122**, 11145 (2018).
[21]J. Hong, M. S. Kelley, M. L. Shelby, D. K. Hayes, R. G. Hadt, D. Rimmerman, X. Zhang, and L. X. Chen, ChemSusChem **11**, 2421 (2018).
[22]X.-B. Li, Y.-J. Gao, Y. Wang, F. Zhan, X.-Y. Zhang, Q.-Y. Kong, N.-J. Zhao, Q. Guo, H.-L. Wu, Z.-J. Li, Y. Tao, J.-P. Zhang, B. Chen, C.-H. Tung, and L.-Z. Wu, J. Am. Chem. Soc. **139**, 4789 (2017).
[23]H. Tsai, C. Liu, E. Kinigstein, M. Li, S. Tretiak, M. Cotlet, X. Ma, X. Zhang, and W. Nie, Adv. Sci. **7**, 1903202 (2020).
[24]P. A. Elzinga, R. J. Kneisler, F. E. Lytle, Y. Jiang, G. B. King, and N. M. Laurendeau, Appl. Opt. **26**, 4303 (1987).
[25]A. Bartels, F. Hudert, C. Janke, T. Dekorsy, and K. Köhler, Appl. Phys. Lett. **88**, 041117 (2006).
[26]V. A. Stoica, Y.-M. Sheu, D. A. Reis, and R. Clarke, Opt. Express **16**, 2322 (2008).
[27]T. Yasui, E. Saneyoshi, and T. Araki, Appl. Phys. Lett. **87**, 061101 (2005).
[28]M. Chergui, Coord. Chem. Rev. **372**, 52 (2018).
[29]M. Reinhard, G. Auböck, N. A. Besley, I. P. Clark, G. M. Greetham, M. W. D. Hanson-Heine, R. Horvath, T. S. Murphy, T. J. Penfold, M. Towrie, M. W. George, and M. Chergui, J. Am. Chem. Soc. **139**, 7335 (2017).
[30]A. M. March, G. Doumy, A. Andersen, A. Al Haddad, Y. Kumagai, M.-F. Tu, J. Bang, C. Bostedt, J. Uhlig, D. R. Nascimento, T. A. Assefa, Z. Németh, G. Vankó, W. Gawelda, N. Govind, and L. Young, J. Chem. Phys. **151**, 144306 (2019).
[31]C. D. Borsarelli, S. G. Bertolotti, and C. M. Previtali, Photochem. Photobiol. Sci. **2**, 791 (2003).
[32]G. Auböck and M. Chergui, Nat. Chem. **7**, 629 (2015).
[33]C. Liu, J. Zhang, L. M. Lawson Daku, D. Gosztola, S. E. Canton, and X. Zhang, J. Am. Chem. Soc. **139**, 17518 (2017).
[34]W. Gawelda, A. Cannizzo, V.-T. Pham, F. van Mourik, C. Bressler, and M. Chergui, J. Am. Chem. Soc. **129**, 8199 (2007).
[35]K. Haldrup, G. Vankó, W. Gawelda, A. Galler, G. Doumy, A. M. March, E. P. Kanter, A. Bordage, A. Dohn, T. B. van Driel, K. S. Kjær, H. T. Lemke, S. E. Canton, J. Uhlig, V. Sundström, L. Young, S. H. Southworth, M. M. Nielsen, and C. Bressler, J. Phys. Chem. A **116**, 9878 (2012).
[36]W. Gawelda, V.-T. Pham, M. Benfatto, Y. Zaushitsyn, M. Kaiser, D. Grolimund, S. L. Johnson, R. Abela, A. Hauser, C. Bressler, and M. Chergui, Phys. Rev. Lett. **98**, 057401 (2007).
[37]A. Cannizzo, C. J. Milne, C. Consani, W. Gawelda, C. Bressler, F. van Mourik, and M. Chergui, Coord. Chem. Rev. **254**, 2677 (2010).
[38]A. S. Tremsin, J. V. Vallerga, O. H. W. Siegmund, J. Woods, L. E. De Long, J. T. Hastings, R. J. Koch, S. A. Morley, Y.-D. Chuang, and S. Roy, J. Synchrotron Radiat. **28**, 1069 (2021).
[39]A. S. Tremsin, J. V. Vallerga, J. B. McPhate, and O. H. W. Siegmund, Nucl. Instrum. Methods Phys. Res., Sect. A **787**, 20 (2015).
[40]Y. Takagi and S. Adachi, Rev. Sci. Instrum. **70**, 2218 (1999).
[41]J. D. Kafka, J. W. Pieterse, and M. L. Watts, Opt. Lett. **17**, 1286 (1992).
[42]P. A. Elzinga, F. E. Lytle, Y. Jian, G. B. King, and N. M. Laurendeau, Appl. Spectrosc. **41**, 2 (1987).
[43]M. S. Brown, G. J. Fiechtner, J. V. Rudd, D. A. Zimdars, M. Warmuth, and J. R. Gord, Appl. Spectrosc. **60**, 261 (2006).